Modeling the flow characteristics of high-velocity non-Darcy flow in gas reservoirs with heterogeneously distributed fractures

Renshi Nie[1], Chaobin Wang[1], Xiaohui Fan[2], Ming Wang[3], Mingjin Cai[3], Tao Zhang[4], Cong Lu[1], Fanhui Zeng[1]

[1. *National Key Laboratory of Oil & Gas Reservoir Geology and Exploitation, Southwest Petroleum University, Chengdu 610500, China;*

[2. *2. Petrochina Changqing Oilfield Company, Xi'an 710000, China;*

[3. *3. Petrochina Tarim Oilfield Company, Korla 84100, China;*

[4. *4. Xi'an 3-D technology development Co., Ltd, Xi'an 710021, China*]

Abstract: In naturally fractured gas reservoirs with highly heterogeneous fracture distributions, high-velocity non-Darcy (HVND) flow tends to occur near the wellbore, especially in fracture-intensive zones. As flow velocity increases, inertial and nonlinear effects become significant, causing deviation from linear Darcy behavior. The conventional Darcy flow equation neglects these nonlinear factors and thus fails to represent the actual flow conditions accurately. To address this, a dual-porosity, dual-permeability two-region composite model is developed, applying Izbash's equation to the inner HVND zone and Darcy flow to the outer zone. The model incorporates porosity and permeability contrasts between matrix and fractures, along with wellbore storage and skin effects. A semi-analytical solution is obtained using line source function, linearization, Laplace transform, and Stehfest inversion. Bottomhole pressure and derivative curves reveal seven flow stages, including non-Darcy crossflow, transition flow, and Darcy crossflow. The non-Darcy index quantifies HVND intensity; lower values indicate stronger nonlinearity. More intensive fractures enhance interregional transmissibility and storage, amplifying transition-stage responses. The proposed model effectively characterizes HVND behavior in gas reservoirs with spatially heterogeneous fractures, providing a theoretical basis for analyzing complex well test responses.

Keywords：non-Darcy flow；flow model； natural fracture； dual-porosity； gas reservoir

1 Introduction

Compared to crude oil, natural gas has a lower viscosity, which makes it prone to high-velocity non-Darcy flow during its seepage through reservoirs. This phenomenon is particularly pronounced in fractured reservoirs. Conducting research on high-velocity non-Darcy flow models in naturally fractured gas reservoirs is of significant importance, as it enhances our understanding of the high-velocity non-Darcy flow behavior of natural gas in such reservoirs.

Nonlinear seepage phenomena, characterized by non-Darcy flow behavior at high velocities, demonstrate a nonlinear correlation between flow velocity and pressure gradient. Two fundamental equations describe this relationship: the binomial Forchheimer equation and the exponential Izbash equation. The governing partial differential equations for such flow systems derive systematically from mass conservation principles through infinitesimal element analysis, incorporating both the motion equations and the respective equations of state for rock-fluid systems.

Currently, research on high-velocity non-Darcy flow based on the Forchheimer equation is quite extensive, including: The applicability of empirical formulas in the Forchheimer equation was investigated for different porous media[1]; A hydro-mechanical coupled model incorporating non-Darcy flow[2]; The influence of Forchheimer coefficient, fluid viscosity, and other parameters on inertial effects was analyzed based on Buckley–Leverett theory[3] ;a dual-porosity model featuring vugs (inner zone) and natural fractures (outer zone) [4], a dual-porosity reservoir model accounting for high-velocity non-Darcy skin effects[5], homogeneous reservoir vertical well testing models[6]. Following Izbash's seminal 1931 experimental formulation of the exponential high-velocity flow equation, subsequent modeling efforts have produced: Quantification the effects of fracture geometry and fluid inertia on Izbash equation coefficients[7]; A nonlinear flow model for rough fractures that simultaneously considers geometric modifications and inertial effects[8]; An experimental analysis on the parameters of Izbash model[9]; Introducing new parameters to rectify Izbash equation[10], and groundwater/waterflooding models addressing high-velocity flow dynamics[11-14].

Both the Forchheimer equation and the Izbash equation can accurately describe non-Darcy flow in porous media. Although various high-velocity non-Darcy flow models have been proposed for naturally fractured gas reservoirs, they generally neglect the heterogeneous distribution of fractures[15] under dual-porosity conditions. The so-called heterogeneous fracture development refers to the phenomenon where certain reservoir zones exhibit dense

natural fractures while others show sparse fracture networks. To enhance single-well productivity, development wells are predominantly deployed in fracture-dense zones. When wells are located in fracture-dense zones, the distal regions exhibit lower fracture density, and single-well production induces planar radial flow within the formation, collectively manifesting radial composite characteristics centered at the wellbore. Two factors drive this behavior: First, the near-well fracture-dense zones possess far superior petrophysical properties compared to distal regions; second, the steep pressure gradient and high gas flow velocities near the wellbore amplify high-velocity non-Darcy effects in proximal fracture networks.

To address this practical scenario, an innovative dual-porosity/dual-permeability two-zone composite flow model was established based on Izbash's equation, incorporating high-velocity non-Darcy flow in the near-well zone and Darcy flow in the distal zone. Through model solving, characteristic wellbore pressure dynamic response curves were plotted, and the high-velocity non-Darcy flow behavior of natural gas in reservoirs with heterogeneous fracture development was systematically analyzed.

2 Physical modeling

For naturally fractured gas reservoirs with non-uniform fracture development, considering the scenario where the well is drilled in a fracture-developed zone, a physical model of a "dual-dual" two-zone composite formation is established, as shown in Figure 1. The model assumes that the inner zone is the near-wellbore fracture-developed zone with favorable physical properties, while the outer zone has lower fracture development and poorer physical properties. The well produces at a constant rate q_{sc}, with the inner zone exhibiting high-velocity non-Darcy flow and the outer zone exhibiting Darcy flow.

Other basic assumptions of the physical model are as follows:

① The gas reservoir is circular and uniform in thickness h, with an inner-zone radius R. Both the inner and outer zones have the same initial reservoir pressure p_i;

② In the inner zone: Matrix permeability and porosity are k_{1m} and ϕ_{1m} Natural fracture permeability and porosity are k_{1nf} and ϕ_{1f};

③ In the outer zone: Matrix permeability and porosity are k_{2m} and ϕ_{2m} Natural fracture permeability and porosity are k_{2nf} and ϕ_{2f};

④ The boundary conditions of the gas reservoir can be: An infinite-acting boundary/ constant-pressure boundary at distance r_e /closed boundary at distance r_e;

⑤ Wellbore storage effect and skin effect are considered.

3 Mathematical modeling

3.1 The establishment of a dimensionless mathematical model.

Based on the parameter definitions provided in the Parameter definition section and the derivation process detailed in Appendix A, the dimensionless mathematical model can be obtained.

For the non-Darcy flow region.

Fracture subsystem:

$$\frac{\partial^2 \psi_{1\mathrm{nfD}}}{\partial r_{\mathrm{D}}^2}+\frac{1/n}{r_{\mathrm{D}}}\frac{\partial \psi_{1\mathrm{nfD}}}{\partial r_{\mathrm{D}}}+\frac{1}{n}\lambda_{1\mathrm{mnf}}R_{\mathrm{D}}^{\frac{1-n}{n}}r_{\mathrm{D}}^{\frac{n-1}{n}}(\psi_{1\mathrm{mD}}-\psi_{1\mathrm{nfD}}) = \frac{1}{n}R_{\mathrm{D}}^{\frac{1-n}{n}}r_{\mathrm{D}}^{\frac{n-1}{n}}\omega_{1\mathrm{nf}}\frac{\partial \psi_{1\mathrm{nfD}}}{\partial t_{\mathrm{D}}},\quad 1\le r_{\mathrm{D}}\le R_{\mathrm{D}} \tag{1}$$

Matrix subsystem:

$$(1-\omega_{1\mathrm{nf}})\frac{\partial \psi_{1\mathrm{mD}}}{\partial t_{\mathrm{D}}}+\lambda_{1\mathrm{mnf}}(\psi_{1\mathrm{mD}}-\psi_{1\mathrm{nfD}})=0 \tag{2}$$

For the Darcy flow region.

Fracture subsystem:

$$\frac{\partial^2 \psi_{2\mathrm{nfD}}}{\partial r_{\mathrm{D}}^2}+\frac{1}{r_{\mathrm{D}}}\frac{\partial \psi_{2\mathrm{nfD}}}{\partial r_{\mathrm{D}}}+\lambda_{2\mathrm{mnf}}(\psi_{2\mathrm{mD}}-\psi_{2\mathrm{nfD}}) = \frac{M_{12}}{\omega_{12}}\omega_{2\mathrm{nf}}\frac{\partial \psi_{2\mathrm{nfD}}}{\partial t_{\mathrm{D}}},\qquad r_{\mathrm{D}}\ge R_{\mathrm{D}} \tag{3}$$

Matrix subsystem:

$$(1-\omega_{2\mathrm{nf}})\frac{M_{12}}{\omega_{12}}\frac{\partial \psi_{2\mathrm{mD}}}{\partial t_{\mathrm{D}}}+\lambda_{2\mathrm{mnf}}(\psi_{2\mathrm{mD}}-\psi_{2\mathrm{nfD}})=0 \tag{4}$$

Initial condition:

$$\psi_{1\mathrm{nfD}}\big|_{t_{\mathrm{D}}=0}=\psi_{1\mathrm{mD}}\big|_{t_{\mathrm{D}}=0}=\psi_{2\mathrm{nfD}}\big|_{t_{\mathrm{D}}=0}=\psi_{2\mathrm{mD}}\big|_{t_{\mathrm{D}}=0}=0 \tag{5}$$

Inner boundary condition:

$$\lim_{r_{\mathrm{D}}\to 0} r_{\mathrm{D}}\frac{\partial \psi_{1\mathrm{nfD}}}{\partial r_{\mathrm{D}}}=-\tilde{q}_{\mathrm{D}}R_{\mathrm{D}}^{\frac{1-n}{n}} \tag{6}$$

Interaction conditions.

Pressure continuity condition:

$$\psi_{1\mathrm{nfD}}\Big|_{r_\mathrm{D}=R_\mathrm{D}} = \psi_{2\mathrm{nfD}}\Big|_{r_\mathrm{D}=R_\mathrm{D}} \tag{7}$$

Gas-rate continuity condition:

$$\left.\frac{\partial \psi_{1\mathrm{nfD}}}{\partial r_\mathrm{D}}\right|_{r_\mathrm{D}=R_\mathrm{D}} = \frac{1}{M_{12}}\left.\frac{\partial \psi_{2\mathrm{nfD}}}{\partial r_\mathrm{D}}\right|_{r_\mathrm{D}=R_\mathrm{D}} \tag{8}$$

Outer boundary conditions.

① Infinite boundary:

$$\lim_{r\to\infty}\psi_{2\mathrm{nfD}} = 0 \tag{9}$$

② Constant-pressure boundary:

$$\psi_{2\mathrm{nfD}}\Big|_{r_\mathrm{D}=r_{e\mathrm{D}}} = 0 \tag{10}$$

③ Closed boundary:

$$\left.\frac{\partial \psi_{2\mathrm{nfD}}}{\partial r_\mathrm{D}}\right|_{r_\mathrm{D}=r_{e\mathrm{D}}} = 0 \tag{11}$$

3.2 Mathematical model solutions

The dimensionless equations are subjected to a Laplace transform with respect to t_D using Equation(12).

$$\overline{\psi}_\mathrm{D}(r_\mathrm{D},u) = \overline{p}_\mathrm{D}(r_\mathrm{D},u) = \int_0^\infty \psi_\mathrm{D}(r_\mathrm{D},t_\mathrm{D})e^{-ut_\mathrm{D}}dt_\mathrm{D} \tag{12}$$

For the non-Darcy flow region.

Fracture subsystem:

$$\begin{aligned}\frac{\partial^2 \overline{\psi}_{1\mathrm{nfD}}}{\partial r_\mathrm{D}^2} + \frac{1/n}{r_\mathrm{D}}\frac{\partial \overline{\psi}_{1\mathrm{nfD}}}{\partial r_\mathrm{D}} + \frac{1}{n}\lambda_{1\mathrm{mnf}} R_\mathrm{D}^{\frac{1-n}{n}} r_\mathrm{D}^{\frac{n-1}{n}}(\overline{\psi}_{1\mathrm{mD}} - \overline{\psi}_{1\mathrm{nfD}}) \\ = u\frac{1}{n}\omega_{1\mathrm{nf}} R_\mathrm{D}^{\frac{1-n}{n}} r_\mathrm{D}^{\frac{n-1}{n}}\overline{\psi}_{1\mathrm{nfD}}, \quad 1 \le r_\mathrm{D} \le R_\mathrm{D}\end{aligned} \tag{13}$$

Matrix subsystem:

$$u(1-\omega_{1\mathrm{nf}})\overline{\psi}_{1\mathrm{mD}} + \lambda_{1\mathrm{mnf}}(\overline{\psi}_{1\mathrm{mD}} - \overline{\psi}_{1\mathrm{nfD}}) = 0 \tag{14}$$

For the Darcy flow region.

Fracture subsystem:

$$\frac{\partial^2\bar{\psi}_{2\mathrm{nfD}}}{\partial r_{\mathrm{D}}^2}+\frac{1}{r_{\mathrm{D}}}\frac{\partial\bar{\psi}_{2\mathrm{nfD}}}{\partial r_{\mathrm{D}}}+\lambda_{2\mathrm{mnf}}(\bar{\psi}_{2\mathrm{mD}}-\bar{\psi}_{2\mathrm{nfD}})=u\frac{M_{12}}{\omega_{12}}\omega_{2\mathrm{nf}}\bar{\psi}_{2\mathrm{nfD}},\qquad r_{\mathrm{D}}\geq R_{\mathrm{D}} \tag{15}$$

Matrix subsystem:

$$(1-\omega_{2\mathrm{nf}})\frac{M_{12}}{\omega_{12}}u\bar{\psi}_{2\mathrm{mD}}+\lambda_{2\mathrm{mnf}}(\bar{\psi}_{2\mathrm{mD}}-\bar{\psi}_{2\mathrm{nfD}})=0 \tag{16}$$

Inner boundary condition:

$$\lim_{r_{\mathrm{D}}\to 0} r_{\mathrm{D}}\frac{\partial\bar{\psi}_{1\mathrm{nfD}}}{\partial r_{\mathrm{D}}}=-\bar{\tilde{q}}_{\mathrm{D}}R_{\mathrm{D}}^{\frac{1-n}{n}} \tag{17}$$

Interaction conditions.

Pressure continuity condition:

$$\bar{\psi}_{1\mathrm{nfD}}\Big|_{r_{\mathrm{D}}=R_{\mathrm{D}}}=\bar{\psi}_{2\mathrm{nfD}}\Big|_{r_{\mathrm{D}}=R_{\mathrm{D}}} \tag{18}$$

Gas-rate continuity condition:

$$\frac{\partial\bar{\psi}_{1\mathrm{nfD}}}{\partial r_{\mathrm{D}}}\bigg|_{r_{\mathrm{D}}=R_{\mathrm{D}}}=\frac{1}{M_{12}}\frac{\partial\bar{\psi}_{2\mathrm{nfD}}}{\partial r_{\mathrm{D}}}\bigg|_{r_{\mathrm{D}}=R_{\mathrm{D}}} \tag{19}$$

Outer boundary conditions.

① Infinite boundary:

$$\lim_{r_{\mathrm{D}}\to\infty}\bar{\psi}_{2\mathrm{nfD}}=0 \tag{20}$$

② Constant-pressure boundary:

$$\bar{\psi}_{2\mathrm{nfD}}\Big|_{r_{\mathrm{D}}=r_{\mathrm{eD}}}=0 \tag{21}$$

③ Closed boundary:

$$\frac{\partial\bar{\psi}_{2\mathrm{nfD}}}{\partial r_{\mathrm{D}}}\bigg|_{r_{\mathrm{D}}=r_{\mathrm{eD}}}=0 \tag{22}$$

Substituting Equation(14) into Equation (13), the following can be obtained:

$$\frac{\partial^2\bar{\psi}_{1\mathrm{nfD}}}{\partial r_{\mathrm{D}}^2}+\frac{1/n}{r_{\mathrm{D}}}\frac{\partial\bar{\psi}_{1\mathrm{nfD}}}{\partial r_{\mathrm{D}}}-\frac{1}{n}uf(u)R_{\mathrm{D}}^{\frac{1-n}{n}}r_{\mathrm{D}}^{\frac{n-1}{n}}\bar{\psi}_{1\mathrm{nfD}}=0 \tag{23}$$

$$f(u)=\frac{\lambda_{1\mathrm{mnf}}}{\lambda_{1\mathrm{mnf}}+(1-\omega_{1\mathrm{nf}})u}+\omega_{1\mathrm{nf}} \tag{24}$$

Equation (23) is a nonlinear equation. In order to obtain its general solution, we have linearized it, and the process is as follows:

For Equation(23), we define:

$$\frac{1}{n} = m \tag{25}$$

Then, Equation(23) can be rewritten as:

$$\frac{\partial^2 \bar{\psi}_{1\mathrm{nfD}}}{\partial r_{\mathrm{D}}^2} + \frac{m}{r_{\mathrm{D}}} \frac{\partial \bar{\psi}_{1\mathrm{nfD}}}{\partial r_{\mathrm{D}}} - muf(u) R_{\mathrm{D}}^{m-1} r_{\mathrm{D}}^{1-m} \bar{\psi}_{1\mathrm{nfD}} = 0 \tag{26}$$

Further, we define:

$$mR_{\mathrm{D}}^{m-1} = b \tag{27}$$

$$\bar{\psi}_{1\mathrm{nfD}}(r_{\mathrm{D}}) = r_{\mathrm{D}}^{\frac{1-m}{2}} \bar{w}(r_{\mathrm{D}}) \tag{28}$$

Substituting Equations(27) and (28) into Equation(26), we obtain:

$$\frac{\partial^2 \bar{w}}{\partial r_{\mathrm{D}}^2} + \frac{1}{r_{\mathrm{D}}} \frac{\partial \bar{w}}{\partial r_{\mathrm{D}}} - \left[\frac{(1-m)^2/4}{r_{\mathrm{D}}^2} + buf(u) r_{\mathrm{D}}^{1-m} \right] \bar{w} = 0, \quad 1 \le r_{\mathrm{D}} \le R_{\mathrm{D}} \tag{29}$$

Define ρ as：

$$\rho = \frac{2}{2+1-m} r_{\mathrm{D}}^{\frac{2+1-m}{2}} \tag{30}$$

Substituting Equation (30) into Equation (29), we obtain:

$$\frac{\partial^2 \bar{w}}{\partial \rho^2} + \frac{1}{\rho} \frac{\partial \bar{w}}{\partial \rho} - \left[\frac{v^2}{\rho^2} + buf(u) \right] \bar{w} = 0, \qquad 1 \le r_{\mathrm{D}} \le R_{\mathrm{D}} \tag{31}$$

Based on the properties of the Bessel equation, the general solution to Equation(31) is:

$$\bar{w} = A_1 \mathrm{I}_v \left(\sqrt{buf(u)} \rho \right) + B_1 \mathrm{K}_v \left(\sqrt{buf(u)} \rho \right) \tag{32}$$

Substituting Equations (25)、(27)、(30) and (32) into Equation (28) , the general solution for the non-Darcy region in Equation (23) is obtained as:

$$\bar{\psi}_{1\mathrm{nfD}} = r_{\mathrm{D}}^{\alpha} \left[A_1 \mathrm{I}_v \left(\frac{\gamma_1}{\beta} r_{\mathrm{D}}^{\beta} \right) + B_1 \mathrm{K}_v \left(\frac{\gamma_1}{\beta} r_{\mathrm{D}}^{\beta} \right) \right] \tag{33}$$

Where:

$$\alpha=\frac{n-1}{2n} \tag{34}$$

$$\beta=\frac{3n-1}{2n} \tag{35}$$

$$v=\frac{n-1}{3n-1} \tag{36}$$

$$\gamma_1=\sqrt{\frac{1}{n}R_{\mathrm{D}}^{\frac{1-n}{n}}uf(u)} \tag{37}$$

The general solution for the Darcy region is:

$$\bar{\psi}_{2\mathrm{nfD}}=A_2\mathrm{I}_0\left(\gamma_2 r_{\mathrm{D}}\right)+B_2\mathrm{K}_0\left(\gamma_2 r_{\mathrm{D}}\right) \tag{38}$$

Where:

$$\gamma_2=\sqrt{u\frac{M_{12}}{\omega_{12}}\left[\frac{\lambda_{2\mathrm{mnf}}+\frac{M_{12}}{\omega_{12}}u\omega_{2\mathrm{nf}}(1-\omega_{2\mathrm{nf}})}{(1-\omega_{2\mathrm{nf}})\frac{M_{12}}{\omega_{12}}u+\lambda_{2\mathrm{mnf}}}\right]} \tag{39}$$

To determine the coefficients A_1, B_1, A_2 and B_2 in the general solution, it is necessary to incorporate the inner boundary condition Equation (17), the pressure continuity condition Equation (18), Gas-rate continuity condition (19), and the outer boundary conditions Equations (20) to (22)) into the general solution. This process requires the use of the following properties of the Bessel equation:

$$\begin{aligned}&\lim_{z\to\infty}\mathrm{I}_0(z)\to\infty, \qquad \lim_{z\to\infty}\mathrm{K}_0(z)=0\\ &\lim_{z\to 0}\mathrm{I}_1(z)=0, \qquad \lim_{z\to\infty}z\mathrm{K}_1(z)=1\end{aligned} \tag{40}$$

$$\frac{d}{dz}\mathrm{K}_v(z)=-\frac{1}{2}\left[\mathrm{K}_{v-1}(z)+\mathrm{K}_{v+1}(z)\right] \tag{41}$$

$$\frac{d}{dz}\mathrm{I}_v(z)=\frac{1}{2}\left[\mathrm{I}_{v-1}(z)+\mathrm{I}_{v+1}(z)\right] \tag{42}$$

Substituting Equations (20) to (22) into Equation(38) respectively, we obtain:

① Infinite boundary

$$\lim_{r_{\mathrm{D}}\to\infty}A_2\mathrm{I}_0(\gamma_2 r_{\mathrm{D}})+B_2\mathrm{K}_0(\gamma_2 r_{\mathrm{D}})=0 \tag{43}$$

② Constant-pressure boundary

$$A_2 \mathrm{I}_0(\gamma_2 r_{\mathrm{eD}}) + B_2 \mathrm{K}_0(\gamma_2 r_{\mathrm{eD}}) = 0 \tag{44}$$

③ Closed boundary:

$$A_2 \gamma_2 \mathrm{I}_1(\gamma_2 r_{\mathrm{eD}}) - B_2 \gamma_2 \mathrm{K}_1(\gamma_2 r_{\mathrm{eD}}) = 0 \tag{45}$$

For the sake of convenience in solving, the three outer boundary conditions are uniformly rewritten as:

$$A_2 = B_2 D_{\mathrm{k}} \tag{46}$$

$$D_{\mathrm{k}} = \begin{cases} 0 & \text{Infinite boundary} \\ -\dfrac{\mathrm{K}_0(\gamma_2 r_{\mathrm{eD}})}{\mathrm{I}_0(\gamma_2 r_{\mathrm{eD}})} & \text{Constant-pressure boundary} \\ \dfrac{\mathrm{K}_1(\gamma_2 r_{\mathrm{eD}})}{\mathrm{I}_1(\gamma_2 r_{\mathrm{eD}})} & \text{Closed boundary} \end{cases} \tag{47}$$

The infinite boundary condition refers to an idealized state in which the pressure wave has not yet reached the reservoir boundary. A constant-pressure boundary refers to a condition where external energy, such as aquifers or pressure maintenance, keeps the boundary pressure constant. A closed boundary is one where no fluid crosses the boundary.

Substituting Equation (46) into Equation (38), we obtain:

$$\bar{\psi}_{2\mathrm{fD}} = B_2 \left[D_{\mathrm{k}} \mathrm{I}_0(\gamma_2 r_{\mathrm{D}}) + \mathrm{K}_0(\gamma_2 r_{\mathrm{D}}) \right] \tag{48}$$

Substituting the pressure continuity condition Equation (18) into Equations (33) and (48), we obtain:

$$\left(r_{\mathrm{D}}^{\alpha} \left[A_1 \mathrm{I}_v\left(\frac{\gamma_1}{\beta} r_{\mathrm{D}}^{\beta}\right) + B_1 \mathrm{K}_v\left(\frac{\gamma_1}{\beta} r_{\mathrm{D}}^{\beta}\right) \right] \right) \Bigg|_{r_{\mathrm{D}}=R_{\mathrm{D}}} = \left(B_2 \left[D_{\mathrm{k}} \mathrm{I}_0(\gamma_2 r_{\mathrm{D}}) + \mathrm{K}_0(\gamma_2 r_{\mathrm{D}}) \right] \right) \Big|_{r_{\mathrm{D}}=R_{\mathrm{D}}} \tag{49}$$

Substituting the pressure continuity condition Equation (19) into Equations (33) and (48), we obtain:

$$\left(A_1 \left[r_{\mathrm{D}}^{\alpha} \mathrm{I}_v\left(\frac{\gamma_1}{\beta} r_{\mathrm{D}}^{\beta}\right) \right]' + B_1 \left[r_{\mathrm{D}}^{\alpha} \mathrm{K}_v\left(\frac{\gamma_1}{\beta} r_{\mathrm{D}}^{\beta}\right) \right]' \right) \Bigg|_{r_{\mathrm{D}}=R_{\mathrm{D}}} = \frac{1}{M_{12}} B_2 \left[D_{\mathrm{k}} \mathrm{I}_0'(\gamma_2 r_{\mathrm{D}}) + \mathrm{K}_0'(\gamma_2 r_{\mathrm{D}}) \right] \Big|_{r_{\mathrm{D}}=R_{\mathrm{D}}} \tag{50}$$

Equations (49) and (50) can be further expressed as:

$$R_{\mathrm{D}}^{\alpha}\left[A_1\mathrm{I}_v(\frac{\gamma_1}{\beta}R_{\mathrm{D}}^{\beta})+B_1\mathrm{K}_v(\frac{\gamma_1}{\beta}R_{\mathrm{D}}^{\beta})\right]=B_2\left[D_{\mathrm{k}}\mathrm{I}_0(\gamma_2 R_{\mathrm{D}})+\mathrm{K}_0(\gamma_2 R_{\mathrm{D}})\right] \tag{51}$$

$$A_1R_{\mathrm{I}}'+B_1R_{\mathrm{K}}'=\frac{\gamma_2}{M_{12}}B_2\left[D_{\mathrm{k}}\mathrm{I}_1(\gamma_2 R_{\mathrm{D}})-\mathrm{K}_1(\gamma_2 R_{\mathrm{D}})\right] \tag{52}$$

Where:

$$R_{\mathrm{I}}'=\left(r_{\mathrm{D}}{}^{\alpha}\mathrm{I}_v(\frac{\gamma_1}{\beta}r_{\mathrm{D}}^{\beta})\right)'\Big|_{r_{\mathrm{D}}=R_{\mathrm{D}}}=\alpha R_{\mathrm{D}}^{\alpha-1}\mathrm{I}_v(\frac{\gamma_1}{\beta}R_{\mathrm{D}}^{\beta})+\frac{R_{\mathrm{D}}^{\alpha}}{2}\left[\mathrm{I}_{v-1}(\frac{\gamma_1}{\beta}R_{\mathrm{D}}^{\beta})+\mathrm{I}_{v+1}(\frac{\gamma_1}{\beta}R_{\mathrm{D}}^{\beta})\right] \tag{53}$$

$$R_{\mathrm{K}}'=\left(r_{\mathrm{D}}^{\alpha}\mathrm{K}_v(\frac{\gamma_1}{\beta}r_{\mathrm{D}}^{\beta})\right)'\Big|_{r_{\mathrm{D}}=R_{\mathrm{D}}}=\alpha R_{\mathrm{D}}^{\alpha-1}\mathrm{K}_v(\frac{\gamma_1}{\beta}R_{\mathrm{D}}^{\beta})-\frac{R_{\mathrm{D}}^{\alpha}}{2}\left[\mathrm{K}_{v-1}(\frac{\gamma_1}{\beta}R_{\mathrm{D}}^{\beta})+\mathrm{K}_{v+1}(\frac{\gamma_1}{\beta}R_{\mathrm{D}}^{\beta})\right] \tag{54}$$

$$\left[\mathrm{I}_0'(\gamma_2 r_{\mathrm{D}})\right]'\Big|_{r_{\mathrm{D}}=R_{\mathrm{D}}}=\gamma_2\mathrm{I}_1(\gamma_2 R_{\mathrm{D}}) \tag{55}$$

$$\left[\mathrm{K}_0'(\gamma_2 r_{\mathrm{D}})\right]'\Big|_{r_{\mathrm{D}}=R_{\mathrm{D}}}=-\gamma_2\mathrm{K}_1(\gamma_2 R_{\mathrm{D}}) \tag{56}$$

combining Equations(51) and (52), we obtain:

$$C_{\mathrm{k}}=\frac{R_{\mathrm{D}}^{\alpha}\left[A_1\mathrm{I}_v\left(\frac{\gamma_1}{\beta}R_{\mathrm{D}}^{\beta}\right)+B_1\mathrm{K}_v\left(\frac{\gamma_1}{\beta}R_{\mathrm{D}}^{\beta}\right)\right]}{A_1R_{\mathrm{I}}'+B_1R_{\mathrm{K}}'}=\frac{D_{\mathrm{k}}\mathrm{I}_0(\gamma_2 R_{\mathrm{D}})+\mathrm{K}_0(\gamma_2 R_{\mathrm{D}})}{\frac{\gamma_2}{M_{12}}\left[D_{\mathrm{k}}\mathrm{I}_1(\gamma_2 R_{\mathrm{D}})-\mathrm{K}_1(\gamma_2 R_{\mathrm{D}})\right]} \tag{57}$$

From Equation (57), we obtain:

$$A_1=GB_1 \tag{58}$$

Where:

$$G=\frac{\left[R_{\mathrm{D}}^{\alpha}\mathrm{K}_v\left(\frac{\gamma_1}{\beta}R_{\mathrm{D}}^{\beta}\right)-C_{\mathrm{k}}R_{\mathrm{K}}'\right]}{C_{\mathrm{k}}R_{\mathrm{I}}'-R_{\mathrm{D}}^{\alpha}\mathrm{I}_v\left(\frac{\gamma_1}{\beta}R_{\mathrm{D}}^{\beta}\right)} \tag{59}$$

Substituting Equations (58) and (59) into Equation (33), we obtain:

$$\bar{\psi}_{1\mathrm{nfD}}=B_1r_{\mathrm{D}}^{\alpha}\left[\mathrm{K}_v\left(\frac{\gamma_1}{\beta}r_{\mathrm{D}}^{\beta}\right)+G\cdot\mathrm{I}_v\left(\frac{\gamma_1}{\beta}r_{\mathrm{D}}^{\beta}\right)\right] \tag{60}$$

Taking the derivative of Equation (60), we obtain:

$$\frac{\partial \bar{\psi}_{1\mathrm{nfD}}}{\partial r_{\mathrm{D}}} = B_1 \left[G_{\mathrm{k}} + G \cdot G_{\mathrm{m}} \right] \tag{61}$$

Where:

$$G_{\mathrm{k}} = \alpha r_{\mathrm{D}}^{\alpha-1} \mathrm{K}_v \left(\frac{\gamma_1}{\beta} r_{\mathrm{D}}^{\beta} \right) - \frac{r_{\mathrm{D}}^{\alpha}}{2} \left[\mathrm{K}_{v-1} \left(\frac{\gamma_1}{\beta} r_{\mathrm{D}}^{\beta} \right) + \mathrm{K}_{v+1} \left(\frac{\gamma_1}{\beta} r_{\mathrm{D}}^{\beta} \right) \right] \tag{62}$$

$$G_{\mathrm{m}} = \alpha r_{\mathrm{D}}^{\alpha-1} \mathrm{I}_v \left(\frac{\gamma_1}{\beta} r_{\mathrm{D}}^{\beta} \right) + \frac{r_{\mathrm{D}}^{\alpha}}{2} \left[\mathrm{I}_{v-1} \left(\frac{\gamma_1}{\beta} r_{\mathrm{D}}^{\beta} \right) + \mathrm{I}_{v+1} \left(\frac{\gamma_1}{\beta} r_{\mathrm{D}}^{\beta} \right) \right] \tag{63}$$

Substituting Equations (61), (62), and (63) into Equation (17), and combining the properties of Bessel functions, we obtain:

$$B_1 = (1-\alpha) R_{\mathrm{D}}^{\frac{1-n}{n}} \bar{\tilde{q}}_{\mathrm{D}} \tag{64}$$

Substituting Equation (64) into Equation (60), the line source solution for the high-speed non-Darcy flow model of a dual-dual composite region at any location can be obtained, as shown in the following equation:

$$\bar{\psi}_{1\mathrm{nfD}} = \bar{\tilde{q}}_{\mathrm{D}} \left\{ (1-\alpha) R_{\mathrm{D}}^{\frac{1-n}{n}} r_{\mathrm{D}}^{\alpha} \left[\mathrm{K}_v \left(\frac{\gamma_1}{\beta} r_{\mathrm{D}}^{\beta} \right) + G \cdot \mathrm{I}_v \left(\frac{\gamma_1}{\beta} r_{\mathrm{D}}^{\beta} \right) \right] \right\} \tag{65}$$

Generally, for vertical wells, the reference length $L_{\mathrm{ref}}=r_{\mathrm{w}}$, meaning $r_{\mathrm{D}}=1$, and when $\bar{\tilde{q}}_{\mathrm{D}}=1$, the bottomhole pressure solution for the high-speed non-Darcy flow model of a dual-dual composite reservoir can be obtained as:

$$\bar{\psi}_{\mathrm{wD}} = \left\{ (1-\alpha) R_{\mathrm{D}}^{\frac{1-n}{n}} \left[\mathrm{K}_v \left(\frac{\gamma_1}{\beta} \right) + G \cdot \mathrm{I}_v \left(\frac{\gamma_1}{\beta} \right) \right] \right\} \tag{66}$$

Next, using the Duhamel principle, as shown in Equation(67), the Laplace-space solution for the bottomhole pressure, incorporating wellbore storage effects and skin factor, can be obtained:

$$\bar{\psi}_{\mathrm{wD}}(C_{\mathrm{D}}, S, u) = \frac{u\bar{\psi}_{\mathrm{wD}} + S}{u + C_{\mathrm{D}} u^2 (u\bar{\psi}_{\mathrm{wD}} + S)} \tag{67}$$

Equation(66) represents the bottomhole pressure solution in Laplace space. By employing the Stehfest numerical inversion method, the Laplace-space bottomhole pseudo-pressure solution Equation(66) can be inverted to obtain the bottomhole pressure solution in real space.

4 Characteristic curve of high-speed non-Darcy flow

4.1 Flow stage analysis

Using the above model, the dimensionless bottomhole pseudo-pressure in real space is calculated. A log-log coordinate system is plotted with t_D / C_D as the horizontal axis and pseudo-pressure ψ_{wD} and pseudo-pressure derivative $\psi_{wD}' \cdot t_D / C_D$ as the vertical axes, forming the well-testing theoretical type curves[16-21]. The typical flow characteristics and parameter sensitivity of high-speed non-Darcy well-testing curves for the case where the outer region is a dual-porosity medium are analyzed.

Figure 2 shows the high-velocity non-Darcy(HVND) well-testing type curves for a dual-dual composite reservoir under three outer boundary conditions. It can be observed that the well-testing type curves of this model can be divided into seven main flow stages.

Stage I: Wellbore storage effect stage. The pseudo-pressure and pseudo-pressure derivative curves appear as straight lines with a slope of 1.

Stage II: Skin effect stage. Influenced by the skin factor, the pseudo-pressure derivative curve exhibits a hump-like characteristic.

Stage III: Pseudo-steady-state crossflow stage. This stage is characterized by the pseudo-steady-state flow from the matrix system to the fractures in the non-Darcy region. The downward concavity of the pseudo-pressure derivative curve is influenced by the fracture storage ratio ω_{1nf} and the crossflow coefficient λ_{1mnf}.

Stage IV: Transition flow stage. This stage is primarily influenced by the mobility ratio M_{1nf} and the storage ratio ω_{12}. The pseudo-pressure derivative exhibits an upward trend in its shape.

Stage V: Crossflow stage in the Darcy region. This stage represents the flow from the matrix system to the fractures in the Darcy region. The pseudo-pressure derivative curve shows a second downward concavity, controlled by the fracture storage ratio ω_{2nf} and the crossflow coefficient λ_{2mnf}.

Stage VI: Global radial flow stage. During this stage, the pseudo-pressure derivative curve manifests as a horizontal line.

Stage VII: Boundary response stage. This stage is primarily influenced by the nature of

the outer boundary.

①: Reflects a closed boundary. Both the pseudo-pressure and pressure derivative curves rise and form a straight line with a slope of 1.

②: Reflects an infinite boundary. The pseudo-pressure derivative curve appears as a horizontal line with a value of 0.5.

③: Reflects a constant-pressure boundary. The pseudo-pressure derivative curve exhibits a downward trend.

4.2 Impact of the parameters

Figure 3 illustrates the influence of the high-speed non-Darcy flow index n on the well-testing type curves for a dual-dual composite reservoir. It can be observed that the flow index n is a critical parameter affecting the characteristics of high-speed non-Darcy flow. When the value of n is larger, the curve position is lower; conversely, when n is smaller, the curve position is higher. This indicates that under significant high-speed non-Darcy effects, more energy is consumed for the same production rate. Notably, when n=1, the high-speed non-Darcy flow degenerates into Darcy flow, and the corresponding curve position reaches its lowest point.

Figure 4 illustrates the influence of the radius R_D of the high-speed non-Darcy flow region on the well-testing type curves for a dual-dual composite reservoir. As R_D increases, the duration of high-speed non-Darcy flow is prolonged, and the onset of Darcy flow is delayed. Conversely, when R_D is smaller, the duration of high-speed non-Darcy flow is shortened, and Darcy flow appears earlier. Notably, when R_D takes a larger value, the model can approximately simulate the high-speed non-Darcy flow characteristics of the entire reservoir.

Figure 5 illustrates the influence of the fracture storage ratio in the high-speed non-Darcy region on the well-testing type curves for a dual-dual composite reservoir. During the pseudo-steady-state crossflow flow from the matrix to the fractures, the well-testing curves exhibit a downward concavity. When the fracture storage ratio is larger, the downward concavity becomes narrower and shallower, reflecting a reduced amount of gas stored in the matrix system. Conversely, when the fracture storage ratio is smaller, the downward concavity becomes wider and deeper, indicating an increased amount of gas stored in the matrix system. When the fracture storage ratio equals 1, the model degenerates into a high-speed non-Darcy flow model

for a homogeneous-dual composite reservoir, and the corresponding curve represents the well-testing curve for the homogeneous-dual composite reservoir model.

Figure 6 illustrates the influence of the crossflow coefficient in the high-speed non-Darcy region on the well-testing type curves for a dual-dual composite reservoir. As the crossflow coefficient increases, the fluid exchange between the matrix system and the fracture system occurs earlier, causing the downward concavity in the pseudo-pressure derivative curve to shift to the left. Conversely, when the crossflow coefficient is smaller, the fluid exchange is delayed, and the downward concavity shifts to the right.

Figure 7 illustrates the influence of the mobility ratio M_{12} on the high-speed non-Darcy well-testing type curves for a dual-dual composite reservoir. The mobility ratio directly affects the shape of the curves in the Darcy flow region.

When the mobility ratio is larger, it indicates poorer reservoir properties in the Darcy flow region, resulting in a relatively higher position of the well-testing curves.

Conversely, when the mobility ratio is smaller, it signifies better reservoir properties in the Darcy flow region, leading to a lower position of the well-testing curves.

Figure 8 illustrates the influence of the Storage Coefficient ω_{12} on the high-speed non-Darcy well-testing type curves for a dual-dual composite reservoir. The storage coefficient reflects the difference in storage capacity between the high-speed non-Darcy flow region and the Darcy flow region. When the storage coefficient is larger, the storage capacity of the high-speed non-Darcy region is higher than that of the Darcy flow region, causing the pseudo-pressure derivative curve to rise and form a "hump" characteristic. Conversely, when the storage coefficient is smaller, the storage capacity of the high-speed non-Darcy region is lower than that of the Darcy flow region, resulting in a downward concavity in the pseudo-pressure derivative curve.

Figure 9 illustrates the influence of the fracture storage ratio $\omega_{2\mathrm{nf}}$ in the Darcy flow region on the high-speed non-Darcy well-testing type curves. During the pseudo-steady-state crossflow gas permeates from the matrix to the fracture system, the curves exhibit a distinct downward concavity. As the fracture storage ratio increases, the second downward concavity becomes narrower and shallower, indicating a reduced amount of gas stored in the matrix system of the Darcy region. Conversely, when the fracture storage ratio decreases, the second downward concavity becomes wider and deeper, reflecting an increased amount of gas stored in the matrix system. Notably, when the fracture storage ratio equals 1, the model simplifies to a high-speed non-Darcy flow model for a dual-homogeneous composite reservoir, and the

corresponding curve represents the well-testing curve for the dual-homogeneous composite reservoir model.

Figure 10 illustrates the influence of the crossflow coefficient λ_{2mnf} in the Darcy flow region on the well-testing type curves. The magnitude of the crossflow coefficient directly affects the timing of the pseudo-steady-state crossflow. When the crossflow coefficient is larger, the fluid exchange between the matrix and fracture systems occurs earlier, causing the second downward concavity in the pseudo-pressure derivative curve to shift to the left. Conversely, when the crossflow coefficient is smaller, the fluid exchange is delayed, and the second downward concavity shifts to the right.

4.3 Field application

Well GS3 in a carbonate gas reservoir of the Sichuan Basin was first put into production in 2014. A pressure buildup test was conducted from May 4 to May 24, 2016, with a pre-shut-in production rate of 3.43×10^5 m³/d, pre-shut-in tubing pressure of 54.99 MPa, and a shut-in duration of 167 hours. The measured pressure data from this well were plotted on a log-log curve Figure 11, which exhibited two distinct concave-downward segments. The data were fitted using both the dual-porosity/dual-permeability two-zone composite high-velocity non-Darcy flow model (DPDP-HVND model) and the Darcy model. The Curve reflects five main flow stages: Stage I: Wellbore storage effect stage; Stage II: Skin effect stage; Stage III: Pseudo-steady-state crossflow stage; Stage IV: Transitional flow stage; Stage V: Darcy-region crossflow stage. Under Darcy flow conditions, the pressure drop is linearly related to the flow rate. However, in high-velocity non-Darcy flow, inertial forces appear alongside viscous forces, resulting in a pressure drop that is proportional to the square of the flow rate. Consequently, for the same flow rate, the pressure drop is larger, which manifests as a higher curve on the double-logarithmic plot. It is worth noting that due to constraints imposed by field production requirements, long-duration testing on the case well was not feasible; therefore, only five flow regimes are observed in the curve. The reliability of the model has been validated through the preceding five flow regimes.

Based on the characteristics of the log-log curve and the geological conditions of the well's location, the proposed "dual-dual" composite flow model considering high-velocity non-Darcy flow was applied. Based on preliminary parameters Table 1, the results show good agreement between the theoretical curve and actual measured data points, with the

interpretation results as follows Table 2.

5 Conclusions

(1) The high-speed non-Darcy flow characteristic curve of the dual-dual composite reservoir can be divided into seven distinct flow stages: Stage I Wellbore Storage Effect Stage; Stage II Skin Effect Stage; Stage III Crossflow Stage in the Non-Darcy Region; Stage IV Transition Flow Stage; Stage V Crossflow Flow Stage in the Darcy Region; Stage VI Global Radial Flow Stage; Stage VII Boundary Response Stage

(2) The flow index n is a critical parameter influencing the characteristics of high-speed non-Darcy flow, primarily reflecting the intensity of the high-speed non-Darcy effect of gas in natural fractures. The smaller the value of n, the more pronounced the high-speed non-Darcy effect of gas in the near-well fracture development zone, and the higher the position of the flow characteristic curve. When n=1, the gas flow transitions from high-speed non-Darcy flow to Darcy flow.

(3) The radius R_D of the high-speed non-Darcy flow region significantly affects the duration of high-speed non-Darcy flow and the onset of Darcy flow: The larger the value of R_D, the longer the duration of high-speed non-Darcy flow, and the later the appearance of Darcy flow. When R_D is sufficiently large, the model can approximate the high-speed non-Darcy flow characteristics of the entire reservoir.

(4) The larger the storage ratio ω_{1nf}, the stronger the elastic storage capacity of fractures in the near-well fracture development zone, resulting in a shallower and narrower downward concavity in the derivative curve of the flow characteristic curve. The larger the crossflow coefficient λ_{1mnf}, the earlier the crossflow from the matrix to the fractures occurs, causing the downward concavity in the derivative curve to shift to the left. The influence of the storage ratio and crossflow coefficient in the far-well region with low fracture development on the flow characteristic curve is similar to that in the near-well fracture development zone.

(5) The changes in the mobility ratio M_{12} and storage coefficient ω_{12} between the near-well fracture development zone and the far-well region affect the shape of the flow characteristic curve. The larger the value of M_{12}, the poorer the reservoir properties in the far-well region and the less developed the fractures, resulting in a higher position of the flow characteristic curve. The larger the value of ω_{12}, the greater the storage capacity of the near-well fracture development zone compared to the far-well region, leading to a larger upward amplitude of the derivative curve during the transition flow stage.

(6) Based on the sensitivity analysis results, the curves are qualitatively classified, providing a theoretical explanation for the changes in the type curves caused by variations in well-testing parameters during the production process.

(7) In the field application section, the model demonstrates a good fit with the measured data from Well GS3 on a log-log plot, and relevant formation parameters are obtained. This model can be applied to simulate gas reservoirs with non-uniform fracture development where high-velocity non-Darcy flow occurs.

Parameter definition

Dimensionless Pseudo-Pressure:

$$\psi_{j\mathrm{D}} = \frac{\pi k_{1\mathrm{nf}} h T_{\mathrm{sc}}}{p_{\mathrm{sc}} q_{\mathrm{sc}} T}(\psi_i - \psi_j) \qquad (j = 1\mathrm{m}, 1\mathrm{nf}, 2\mathrm{m}, 2\mathrm{nf}) \tag{1}$$

Dimensionless Time:

$$t_{\mathrm{D}} = \frac{k_{1\mathrm{nf}}}{\mu_{\mathrm{g}}(\phi_{1\mathrm{nf}} C_{1\mathrm{nft}} + \phi_{1\mathrm{m}} C_{1\mathrm{mt}}) L_{\mathrm{ref}}^2} t \tag{2}$$

Dimensionless Distance:

$$r_{\mathrm{D}} = \frac{r}{L_{\mathrm{ref}}} \tag{3}$$

$$R_{\mathrm{D}} = \frac{R}{L_{\mathrm{ref}}} \tag{4}$$

$$r_{\mathrm{eD}} = \frac{r_e}{L_{\mathrm{ref}}} \tag{5}$$

Dimensionless Wellbore Storage Coefficient:

$$C_{\mathrm{D}} = \frac{C}{2\pi(\phi_{1\mathrm{nf}} C_{1\mathrm{nft}} + \phi_{1\mathrm{m}} C_{1\mathrm{mt}}) h L_{\mathrm{ref}}^2} \tag{6}$$

Dimensionless Line Source Flow Rate:

$$\tilde{q}_{\mathrm{D}} = \frac{\tilde{q}}{q_{\mathrm{sc}}} \tag{7}$$

The definitions of other parameters are as follows:
Fracture Storage Ratio in the Non-Darcy Region:

$$\omega_{1\mathrm{nf}} = \frac{\phi_{1\mathrm{nf}} C_{1\mathrm{nft}}}{\phi_{1\mathrm{m}} C_{1\mathrm{mt}} + \phi_{1\mathrm{nf}} C_{1\mathrm{nft}}} \tag{8}$$

Crossflow Coefficient in the Non-Darcy Region:

$$\lambda_{1\mathrm{mnf}} = \alpha_{1\mathrm{m}} \frac{k_{1\mathrm{m}}}{k_{1\mathrm{nf}}} L_{\mathrm{ref}}^2 \tag{9}$$

Fracture Storage Ratio in the Darcy Region:

$$\omega_{2\mathrm{nf}} = \frac{\phi_{2\mathrm{nf}} C_{2\mathrm{nft}}}{\phi_{2\mathrm{m}} C_{2\mathrm{m}} + \phi_{2\mathrm{nf}} C_{2\mathrm{nft}}} \tag{10}$$

Crossflow Coefficient in the Darcy Region:

$$\lambda_{2\mathrm{mnf}} = \alpha_{2\mathrm{m}} \frac{k_{2\mathrm{m}}}{k_{2\mathrm{nf}}} L_{\mathrm{ref}}^2 \tag{11}$$

Mobility Ratio:

$$M_{12} = \frac{M_1}{M_2} = \frac{k_{1\mathrm{nf}} / \mu_{1\mathrm{g}}}{k_{2\mathrm{nf}} / \mu_{2\mathrm{g}}} \tag{12}$$

Storativity Ratio:

$$\omega_{12} = \frac{\phi_{1\mathrm{m}} C_{1\mathrm{mt}} + \phi_{1\mathrm{nf}} C_{1\mathrm{nft}}}{\phi_{2\mathrm{m}} C_{2\mathrm{mt}} + \phi_{2\mathrm{nf}} C_{2\mathrm{nft}}} \tag{13}$$

Symbol Notation

A_1, A_2, A_F —Undetermined Coefficients;

b, B_1, B_2, B_F —Undetermined Coefficients;

c —Empirical Constants; C_K —Parameter; C_D —Dimensionless wellbore storage constant;

D_K —Undetermined Coefficients;

G, G_k, G_m —Undetermined Coefficients;

h —Formation thickness;

I_0 —First Kind, Zero-Order Modified Bessel Function; I_1 —First Kind, First-Order Modified Bessel Function; I_{V-1} —First Kind, v-1-Order Modified Bessel Function; I_V —First Kind, v-Order Modified Bessel Function; I_{V+1} —First Kind, v+1-Order Modified Bessel Function;

k_{1m} —Inner Region Matrix Permeability; k_{1nf} —Inner Region Natural Fracture Permeability; k_{2m} —Outer Region Matrix Permeability; k_{2nf} —Outer Region Natural Fracture Permeability; K_0 —Second Kind, Zero-Order Modified Bessel Function; K_1 —Second Kind, First-Order Modified Bessel Function; K_{V-1} —Second Kind, v-1-Order Modified Bessel Function; K_v —Second Kind, v-Order Modified Bessel Function; K_{V+1} —Second Kind, v+1-Order Modified Bessel Function;

m —Parameter; M_{12} —Mobility Ratio;

n —Empirical Constants;

P_i —Original Formation Pressure;

q_{sc} —Surface flow rate; $\tilde{q}_D$ —Dimensionless Line Source Flow Rate; $\bar{\tilde{q}}_D$ —Dimensionless Line Source Flow Rate in Laplace Space

r_D —Dimensionless Radial Distance; r_e —Boundary Radial Distance; r_{eD} —Dimensionless Reservoir Boundary Radial Distance; R —Inner Region Radius; R_D —Dimensionless Inner Region Radius; R'_I, R'_K —Parameter;

S —Skin Factor;

t_D —Dimensionless Time;

u —Laplace Variable;

v —Seepage Velocity;

$\bar{w}$ —Parameter;

α , β —Substitution Variable;

γ_1 , γ_2 —Substitution Variable;

λ_{1mnf} —Crossflow Coefficient in the Inner Region; λ_{2mnf} —Crossflow Coefficient in the Outer Region;

ρ —Parameter;

ϕ_{1m} —Inner Region Matrix Porosity; ϕ_{1f} —Inner Region Fracture Porosity; ϕ_{2m} —Outer Region Matrix Porosity; ϕ_{2f} —Outer Region Fracture Porosity;

ψ_{1nfd} —Dimensionless Natural Fracture System Pseudo-Pressure in the Inner Region; ψ_{2nfd} —Dimensionless Natural Fracture System Pseudo-Pressure in the Outer Region; ψ_{1md} —Dimensionless Matrix System Pseudo-Pressure in the Inner Region; ψ_{2md} —Dimensionless Matrix System Pseudo-Pressure in the Outer Region; $\bar{\psi}_{1nfd}$ —Dimensionless Natural Fracture System Pseudo-Pressure in Laplace Space in the Inner Region; $\bar{\psi}_{2nfd}$ —Dimensionless Natural Fracture System Pseudo-Pressure in Laplace Space in the Outer Region; $\bar{\psi}_{1md}$ —Dimensionless Matrix System Pseudo-Pressure in Laplace Space in the Inner Region; $\bar{\psi}_{2md}$ —Dimensionless Matrix System Pseudo-Pressure in Laplace Space in the Outer Region; $\bar{\psi}_{wD}$ —Dimensionless Bottomhole Pseudo-Pressure in Laplace Space

ω_{1nf} —Inner Region Fracture Storage Ratio; ω_{2nf} —Outer Region Fracture Storage Ratio; ω_{1m} —Inner Region Matrix Storage Ratio; ω_{2m} —Outer Region Matrix Storage Ratio; ω_{12} —Storage coefficient.

Appendix A

Non-Darcy flow region seepage control equation derivation is as follows:

Basic assumptions: The entire flow process is assumed to be isothermal (i.e., other parameters are unaffected by temperature); the fluid is a single-phase ideal gas, with its density dependent solely on pressure; both the reservoir and the gas are slightly compressible, and the compressibility coefficients of the fractures and the matrix are considered constant.

(1) According to the principle of mass conservation for gas flow, the continuity equation for the natural fracture system can be obtained as:

$$\frac{1}{r}\frac{\partial}{\partial r}\left(r\rho_{\mathrm{g}}v_{\mathrm{g}}\right)+\frac{\partial}{\partial t}\left(\rho_{\mathrm{g}}\phi_{1\mathrm{nf}}\right)-q_{\mathrm{mg}}=0 \tag{A-1}$$

(2) The continuity equation for the matrix system[22]:

$$\frac{\partial}{\partial t}\left(\rho_{\mathrm{g}}\phi_{1\mathrm{m}}\right)+q_{\mathrm{mg}}=0 \tag{A-2}$$

(3) The pseudo-steady-state crossflow equation from the matrix system to the natural fracture system:

$$q_{\mathrm{mg}}=\alpha_{1\mathrm{m}}\rho_{\mathrm{g}}\frac{k_{1\mathrm{m}}}{\mu_{\mathrm{g}}}\left(p_{1\mathrm{m}}-p_{1\mathrm{nf}}\right) \tag{A-3}$$

(4) Equation of motion:

$$v_{\mathrm{g}}=c\left|\frac{\partial p_{1\mathrm{nf}}}{\partial r}\right|^{n} \tag{A-4}$$

(5) Equation of state.

The equation of state for gas:

$$\rho_{\mathrm{g}}=\frac{p_{1\mathrm{nf}}M}{ZRT} \tag{A-5}$$

Equation of state for rock.

① The natural fracture system:

$$\phi_{1\mathrm{nf}}=\phi_{1\mathrm{nf0}}\left[1+C_{1\mathrm{nf}}\left(p_{1\mathrm{nf}}-p_{0}\right)\right] \tag{A-6}$$

② Matrix system:

$$\phi_{1\mathrm{m}}=\phi_{1\mathrm{m0}}\left[1+C_{1\mathrm{m}}\left(p_{1\mathrm{m}}-p_{0}\right)\right] \tag{A-7}$$

(5) Natural gas compressibility factor:

$$C_{\mathrm{g}}=-\frac{1}{V}\left(\frac{\partial V}{\partial p}\right)_{T}=\frac{1}{p}-\frac{1}{Z}\frac{\partial Z}{\partial p} \tag{A-8}$$

Substituting Equations (A-4) and (A-5) into Equation (A-1), the left-hand side of the equation is:

$$\frac{1}{r}\frac{\partial}{\partial r}(\rho_g r v_g)=\frac{1}{r}\frac{\partial}{\partial r}\left(rc(\frac{\partial p_{1nf}}{\partial r})^n\frac{p_{1nf}}{Z}\frac{M}{RT}\right)$$
$$=nc\left(\frac{\partial p_{1nf}}{\partial r}\right)^{n-1}\frac{M}{RT}\frac{p_{1nf}}{Z}\frac{\partial^2 p_{1nf}}{\partial r^2}+\frac{1}{r}c\frac{p_{1nf}}{Z}\frac{M}{RT}\left(\frac{\partial p_{1nf}}{\partial r}\right)^n \quad \text{(A-9)}$$
$$+\frac{1}{r}\frac{1}{Z^2}\left(\mathrm{Z}-p\frac{\partial Z}{\partial p}\right)\frac{M}{RT}c\left(\frac{\partial p_{1nf}}{\partial r}\right)^2\left(\frac{\partial p_{1nf}}{\partial r}\right)^{n-1}$$

when the values of c and $\frac{\partial p_{1f}}{\partial_r}$ are small, $\frac{\partial p_{1f}}{\partial_r}$ □ $\left(\frac{\partial p_{1f}}{\partial_r}\right)^2$ the third term on the right-hand side of Equations. (A.9) can be ignored. Equations. (A.9) can be rewritten as:

$$\frac{1}{r}\frac{\partial}{\partial r}(\rho_g r v_g)=nc\frac{M}{RT}\left(\frac{\partial p_{1nf}}{\partial r}\right)^{n-1}\frac{p_{1nf}}{Z}\frac{\partial^2 p_{1nf}}{\partial r^2}+\frac{1}{r}c\frac{p_{1nf}}{Z}\frac{M}{RT}\left(\frac{\partial p_{1nf}}{\partial r}\right)^n \quad \text{(A-10)}$$

Substituting Equations (A-5) and (A-6) into Equation (A-1), the second term on the left-hand side of the equation is:

$$\frac{\partial(\rho_g\phi_{1nf})}{\partial t}=\frac{\partial\left(\frac{p_{1nf}}{Z}\frac{M}{RT}\phi_{1nf0}(1+C_{1nf}(p_{1nf}-p_0))\right)}{\partial t}$$
$$=\frac{\frac{M}{RT}\partial\left(\frac{p_{1nf}}{Z}\phi_{1nf0}(1+C_{1nf}(p_{1nf}-p_0))\right)}{\partial p_{1nf}}\frac{\partial p_{1nf}}{\partial t} \quad \text{(A-11)}$$
$$=\frac{M}{RT}\left(\phi_{1nf0}C_{1nf}\frac{p_{1nf}}{Z}+\phi_{1nf0}(1+C_{1nf}(p_{1nf}-p_0))\left[\frac{1}{Z}-p_{1nf}\frac{1}{Z^2}\frac{\partial Z}{\partial p_{1nf}}\right]\right)\frac{\partial p_{1nf}}{\partial t}$$
$$=\frac{M}{RT}\phi_{1nf0}\frac{p_{1nf}}{Z}\left(C_{1nf}+C_g(1+C_{1nf}(p_{1nf}-p_0))\right)\frac{\partial p_{1nf}}{\partial t}$$

In the above equation, where ϕ_{1nf0} and p_0 are reference values, taken as ϕ_{1nf} and p_{1nf} respectively, Equation (A-11) can be further expressed as:

$$\frac{\partial(\rho_g\phi_{1nf})}{\partial t}=\frac{M}{RT}\phi_{1nf}\frac{p_{1nf}}{Z}\left(C_{1nf}+C_g\right)\frac{\partial p_{1nf}}{\partial t}=\frac{M}{RT}\frac{p_{1nf}}{Z}\phi_{1nf}C_{1nft}\frac{\partial p_{1nf}}{\partial t} \quad \text{(A-12)}$$

Based on Equations (A-3), (A-10), and (A-12), it can be obtained that:

$$\frac{p_{1nf}}{Z}\frac{\partial^2 p_{1nf}}{\partial r^2}+\frac{1/n}{r}\frac{p_{1nf}}{Z}\frac{\partial p_{1nf}}{\partial r}+\alpha_{1m}\frac{k_{1m}}{\mu_g nc}\frac{p_{1nf}}{Z}\left(\frac{\partial p_{1nf}}{\partial r}\right)^{1-n}(p_{1m}-p_{1nf})$$
$$=\frac{1}{n}\frac{1}{c}C_{1nft}\phi_{1nf}\left(\frac{\partial p_{1nf}}{\partial r}\right)^{1-n}\frac{p_{1nf}}{Z}\frac{\partial p_{1nf}}{\partial t},\qquad r_w\le r\le R \quad \text{(A-13)}$$

Based on Equations (A-2), (A-3), (A-4), (A-5), and (A-8), it can be obtained that:

$$\phi_{1m}C_{1mt}\frac{p_{1nf}}{Z}\frac{\partial p_{1m}}{\partial t}+\alpha_{1m}\frac{k_{1m}}{\mu_g}\frac{p_{1nf}}{Z}(p_{1m}-p_{1nf})=0 \quad \text{(A-14)}$$

Then, Equations (A-13) and (A-14) are the seepage control equations for the non-Darcy flow region considering the exponential equation. However, Equation (A-13) is a nonlinear

equation, and to obtain its analytical solution, the equation is processed.

From Equation (A-4), it can be seen that:

$$\left(\frac{\partial p_{1\mathrm{nf}}}{\partial r}\right)^{n}=\frac{1}{c}\left(\frac{q_{\mathrm{sc}}B_{\mathrm{g}}}{2\pi rh}\right) \tag{A-15}$$

Substituting Equation (A-15) into Equation (A-13), we can obtain:

$$\begin{aligned}&\frac{p_{1\mathrm{nf}}}{Z}\frac{\partial^{2}p_{1\mathrm{nf}}}{\partial r^{2}}+\frac{1/n}{r}\frac{p_{1\mathrm{nf}}}{Z}\frac{\partial p_{1\mathrm{nf}}}{\partial r}+\alpha_{1\mathrm{m}}\frac{k_{1\mathrm{m}}}{\mu_{\mathrm{g}}nc}\frac{p_{1\mathrm{nf}}}{Z}\left(\frac{q_{\mathrm{sc}}B_{\mathrm{g}}}{2\pi rhc}\right)^{\frac{1-n}{n}}(p_{1\mathrm{m}}-p_{1\mathrm{nf}})\\&=\frac{1}{n}\frac{1}{c}C_{1\mathrm{nft}}\phi_{1\mathrm{nf}}\left(\frac{q_{\mathrm{sc}}B_{\mathrm{g}}}{2\pi rhc}\right)^{\frac{1-n}{n}}\frac{p_{1\mathrm{nf}}}{Z}\frac{\partial p_{1\mathrm{nf}}}{\partial t},\qquad r_{\mathrm{w}}\le r\le R\end{aligned} \tag{A-16}$$

Here, referencing the solution method for non-Newtonian fluid seepage by Ikuko-Ramey[23, 24], the characteristic permeability k^{*}_{1} and apparent permeability $k_{1\mathrm{a}}$ are defined, with the relationship as follows:

$$k_{1}^{*}=\mu c\left(\frac{q_{\mathrm{sc}}B_{\mathrm{g}}}{2\pi chr_{w}}\right)^{\frac{1-n}{n}} \tag{A-17}$$

$$\frac{k_{1a}}{k_{1}^{*}}=\left(\frac{r}{r_{\mathrm{w}}}\right)^{\frac{1-n}{n}} \tag{A-18}$$

The purpose of the above treatment is to equate the inertial resistance during high-speed non-Darcy seepage to the change in apparent permeability $k_{1\mathrm{a}}$. Due to the high gas velocity near the wellbore, the inertial resistance is large, and the apparent permeability is smaller. Conversely, in the region far from the wellbore, the gas velocity is relatively slower, the inertial resistance is small, and the apparent permeability is larger. At the interface between the non-Darcy seepage region and the Darcy seepage region, the high-speed non-Darcy effect is very weak, and the apparent permeability approaches the formation permeability. Therefore, the permeability at the interface is:

$$k_{1\mathrm{nf}}\approx k_{1a}\big|_{r=R}=k_{1}^{*}R^{\frac{1-n}{n}} \tag{A-19}$$

To simplify the solution of the model, the definition of pseudo-pressure is introduced here[25]:

$$\psi_{1}(p_{1})=\int_{0}^{p_{1}}\frac{2p_{1}}{\mu_{1}Z}dp \tag{A-20}$$

Using dimensionless parameters (refer to the parameter definition section), the dimensionless control equation for the non-Darcy flow region can ultimately be obtained as:

$$\begin{aligned}&\frac{\partial^{2}\psi_{1\mathrm{nfD}}}{\partial r_{\mathrm{D}}^{2}}+\frac{1/n}{r_{\mathrm{D}}}\frac{\partial\psi_{1\mathrm{nfD}}}{\partial r_{\mathrm{D}}}+\frac{1}{n}\lambda_{1\mathrm{mnf}}R_{\mathrm{D}}^{\frac{1-n}{n}}r_{\mathrm{D}}^{\frac{n-1}{n}}(\psi_{1\mathrm{mD}}-\psi_{1\mathrm{nfD}})\\&=\frac{1}{n}R_{\mathrm{D}}^{\frac{1-n}{n}}r_{\mathrm{D}}^{\frac{n-1}{n}}\omega_{1\mathrm{nf}}\frac{\partial\psi_{1\mathrm{nfD}}}{\partial t_{\mathrm{D}}}\qquad 1\le r_{\mathrm{D}}\le R_{\mathrm{D}}\end{aligned} \tag{A-21}$$

References

1. YUAN, S., LI, Z., XIONG, T., et al. "Quantitative evaluation of forchheimer equation for non-darcy flow in porous media ". *Hydrogeology & Engineering Geology*, 51(3): p. 12–22, (2024), https://doi.org/10.16030/j.cnki.issn.1000-3665.202308015.
2. ZHOU, Y., YANG, D., SUI, Q., et al. "An XFEM-based hydro-mechanical model to consider the non-Darcy flow in complex fracture networks ". *International Journal of Rock Mechanics and Mining Sciences*, 170: p. 105517, (2023), https://doi.org/10.1016/j.ijrmms.2023.105517.
3. WANG, Y., YAO, J., HUANG, Z. "Parameter Effect Analysis of Non-Darcy Flow and a Method for Choosing a Fluid Flow Equation in Fractured Karstic Carbonate Reservoirs ". *Energies*, 15(10), (2022), https://doi.org/10.3390/en15103623.
4. GAO, B., HUANG, Z., YAO, J., et al. "Pressure transient analysis of a well penetrating a filled cavity in naturally fractured carbonate reservoirs ". *Journal of Petroleum Science and Engineering*, 145: p. 392–403, (2016), https://doi.org/10.1016/j.petrol.2016.05.037.
5. ZENG, F., ZHAO, G., XU, X. "Transient Pressure Behaviour Under Non- Darcy Flow, Formation Damage and Their Combined Effect for Dual Porosity Reservoirs ". *Journal of Canadian Petroleum Technology*, 48(07): p. 54–65, (2009), https://doi.org/10.2118/09-07-54.
6. ZENG, F., ZHAO, G. "Semianalytical Model for Reservoirs With Forchheimer's Non-Darcy Flow ". *SPE Reservoir Evaluation & Engineering*, 11(02): p. 280–91, (2008), https://doi.org/10.2118/100540-pa.
7. XING, K., MA, L., QIAN, J., et al. "Experimental and numerical study on the Izbash equation coefficients in rough single fractures ". *Physics of Fluids*, 35(12), (2023), https://doi.org/10.1063/5.0176467.
8. ZHANG, Y., LI, Q. "A nonlinear flow model for rough fractures with geometric heterogeneity based on improved Izbash's law ". *Journal of Hydrology*, 632, (2024), https://doi.org/10.1016/j.jhydrol.2024.130894.
9. PANDEY, S., SHARMA, P. "Experimental study on non-Darcian flow through a single artificial fracture for different fracture apertures and surface roughness ". *Journal of Hydroinformatics*, 25(6): p. 2460–78, (2023), https://doi.org/10.2166/hydro.2023.143.
10. ZHANG, Y., CHAI, J., CAO, C., et al. "Investigating Izbash's law on characterizing nonlinear flow in self-affine fractures ". *Journal of Petroleum Science and Engineering*, 215, (2022), https://doi.org/10.1016/j.petrol.2022.110603.
11. WEN, Z., HUANG, G., ZHAN, H. "Non-Darcian flow to a well in an aquifer-aquitard system ". *Advances in Water Resources*, 31(12): p. 1754–63, (2008), https://doi.org/10.1016/j.advwatres.2008.09.002.
12. WEN, Z., HUANG, G., ZHAN, H. "A numerical solution for non-Darcian flow to a well in a confined aquifer using the power law function ". *Journal of Hydrology*, 364(1-2): p. 99–106, (2009), https://doi.org/10.1016/j.jhydrol.2008.10.009.
13. WEN, Z., WU, F., FENG, Q. "Non-Darcian Flow to a Partially Penetrating Pumping Well in

a Leaky Aquifer Considering the Aquitard-Aquifer Interface Flow ". *Journal of Hydrologic Engineering*, 21(12), (2016), https://doi.org/10.1061/(asce)he.1943-5584.0001446.

14. XIAO, L., YE, M., XU, Y., et al. "A Simplified Solution Using Izbash's Equation for Non-Darcian Flow in a Constant Rate Pumping Test ". *Groundwater*, 57(6): p. 962–8, (2019), https://doi.org/10.1111/gwat.12886.
15. HUAN, J., HE, M., WAN, Z., et al. "Scale effects and spatial distribution characteristics of 3D roughness of natural rock fracture surfaces: statistical analysis ". *Acta Geophysica*, 73(1): p. 83–103, (2025), https://doi.org/10.1007/s11600-024-01397-1.
16. NIE, R., MENG, Y., JIA, Y., et al. "Dual Porosity and Dual Permeability Modeling of Horizontal Well in Naturally Fractured Reservoir ". *Transport in Porous Media*, 92(1): p. 213–35, (2012), https://doi.org/10.1007/s11242-011-9898-3.
17. JIANG, R., ZHANG, F., CUI, Y., et al. "Production performance analysis of fractured vertical wells with SRV in triple media gas reservoirs using elliptical flow ". *Journal of Natural Gas Science and Engineering*, 68, (2019), https://doi.org/10.1016/j.jngse.2019.102925.
18. EGYA, D., CORBETT, P., GEIGER, S., et al. "Calibration of naturally fractured reservoir models using integrated well-test analysis - an illustration with field data from the Barents Sea ". *Petroleum Geoscience*, 28(1), (2022), https://doi.org/10.1144/petgeo2020-042.
19. WEI, C., TAN, Z., HUANG, G., et al. "Generalized Analytical Well-Test Solutions for Vertically Fractured Wells in Commingled Reservoirs ". *Journal of Energy Resources Technology-Transactions of the Asme*, 146(5), (2024), https://doi.org/10.1115/1.4065032.
20. TOHIDI, A., FAHIMIFAR, A., RASOULI, V. "Effect of non-Darcy flow on induced stresses around a wellbore in an anisotropic in-situ stress field ". *Scientia Iranica*, 26(3): p. 1182–93, (2019), https://doi.org/10.24200/sci.2017.4603.
21. BANIASADI, H., RASHIDI, F. "A triple-porosity radial composite model for two-phase well test analysis of volatile oil in fractured-vuggy reservoirs ". *Scientia Iranica*, 28(3): p. 1378–99, (2021), https://doi.org/10.24200/sci.2021.55522.4262.
22. WARREN, J. E., ROOT, P. J. "The Behavior of Naturally Fractured Reservoirs ". *Society of Petroleum Engineers Journal*, 3(03): p. 245–55, (1963), https://doi.org/10.2118/426-pa.
23. IKOKU, C U, RAMEY, H J, JR. "Transient Flow of Non-Newtonian Power-Law Fluids in Porous Media ". *Society of Petroleum Engineers Journal*, 19(03): p. 164–74, (1979), https://doi.org/10.2118/7139-pa.
24. VONGVUTHIPORNCHAI, S., RAGHAVAN, R. "Well Test Analysis of Data Dominated by Storage and Skin: Non-Newtonian Power-Law Fluids ". *SPE Formation Evaluation*, 2(04): p. 618–28, (1987), https://doi.org/10.2118/14454-pa.
25. AL-HUSSAINY, R., RAMEY, H J, JR., CRAWFORD P B. "The Flow of Real Gases Through Porous Media ". *Journal of Petroleum Technology*, 18(05): p. 624–36, (1966),

https://doi.org/10.2118/1243-a-pa.

Author Biographies

Renshi Nie is a Professor at Southwest Petroleum University and a core member of the National Key Laboratory of Oil and Gas Reservoir Geology and Development Engineering. He holds a Ph.D. in Petroleum Engineering and focuses on reservoir engineering, well testing, and transient flow modeling.

Chaobin Wang received his B.Sc. degree in Petroleum Engineering from Southwest Petroleum University, where he is currently pursuing his M.Sc. His research focuses on well test interpretation, non-Darcy flow, and fractured gas reservoirs.

Xiaohui Fan received his Ph.D. in Petroleum Engineering from Southwest Petroleum University. He is currently working at PetroChina Changqing Oilfield Company in Xi'an, China. His research interests include reservoir engineering and field application of well testing technologies.

Ming Wang is currently with PetroChina Tarim Oilfield Company in Korla, China.

Mingjin Cai received his Ph.D. in Petroleum Engineering from Southwest Petroleum University. He is currently with PetroChina Tarim Oilfield Company in Korla, China. His research interests include reservoir development and well performance analysis in complex gas reservoirs.

Tao Zhang is currently working at Xi'an 3-D Technology Development Co., Ltd. in Xi'an, China.

Cong Lu is a Professor and Ph.D. supervisor at Southwest Petroleum University, where he currently serves as the Associate Dean of the School of Petroleum Engineering. He received his B.Sc., M.Sc., and Ph.D. degrees in Petroleum Engineering from Southwest Petroleum University. His research focuses on reservoir stimulation theory and technologies.

Fanhui Zeng is a Professor and Ph.D. supervisor at Southwest Petroleum University, serving as Director of the Intelligent Oil and Gas Engineering Research Center. He holds B.Sc., M.Sc., and Ph.D. degrees from the same university. His research focuses on enhanced oil and gas recovery, AI applications, fracturing acidizing, big data, and optimization.

Figures&Tables

Figure 1 Dual-dual composite gas reservoir model with high-velocity non-Darcy flow

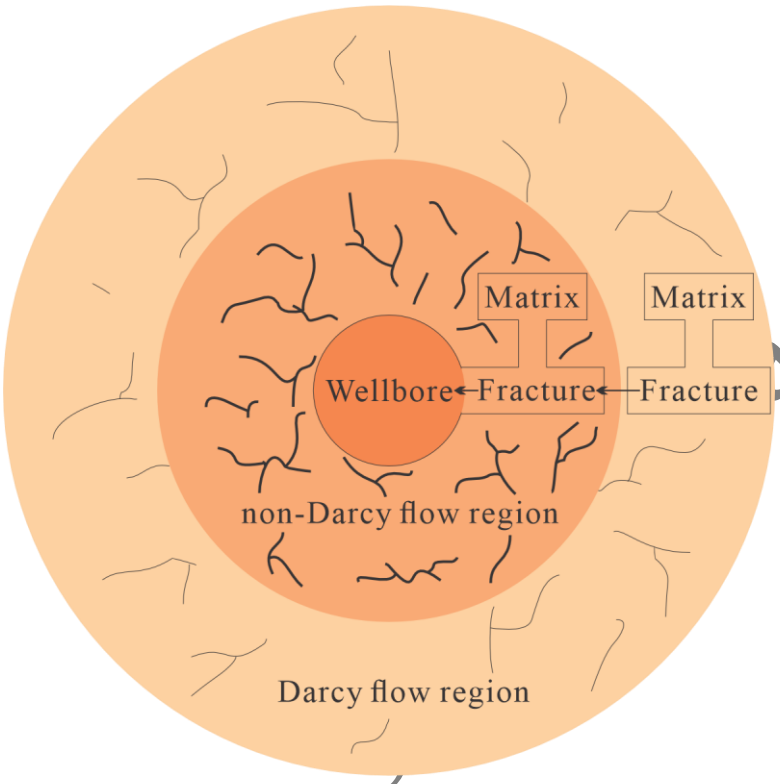

Figure 2 HVND curves for a dual-dual composite reservoir

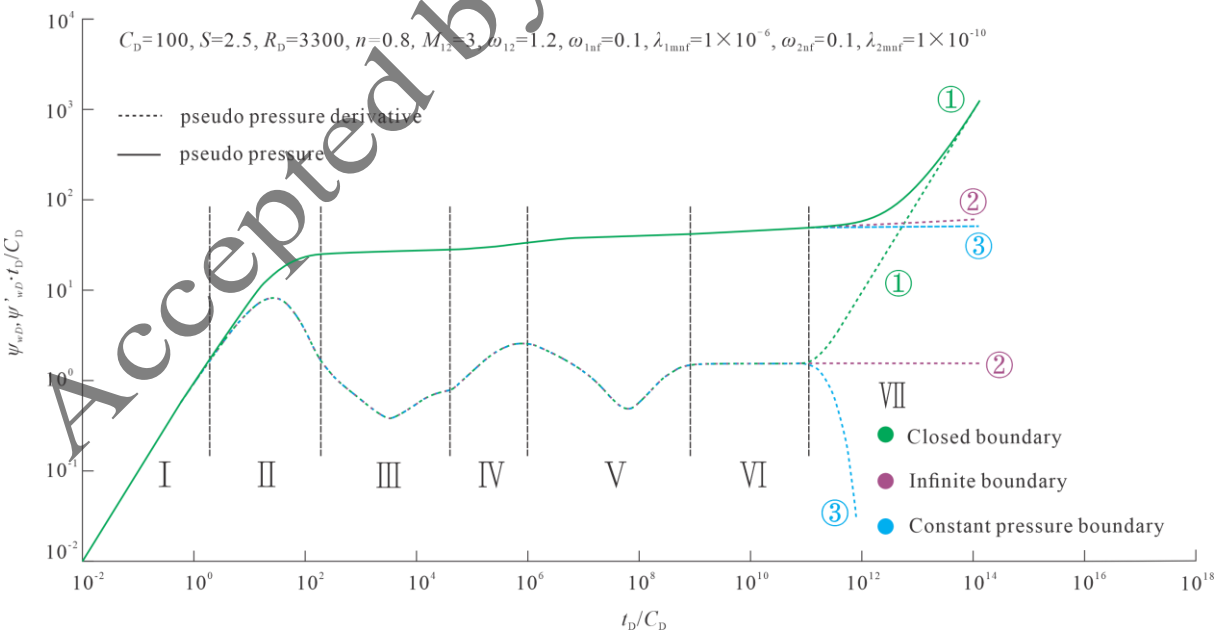

Figure 3 Influence of the flow index

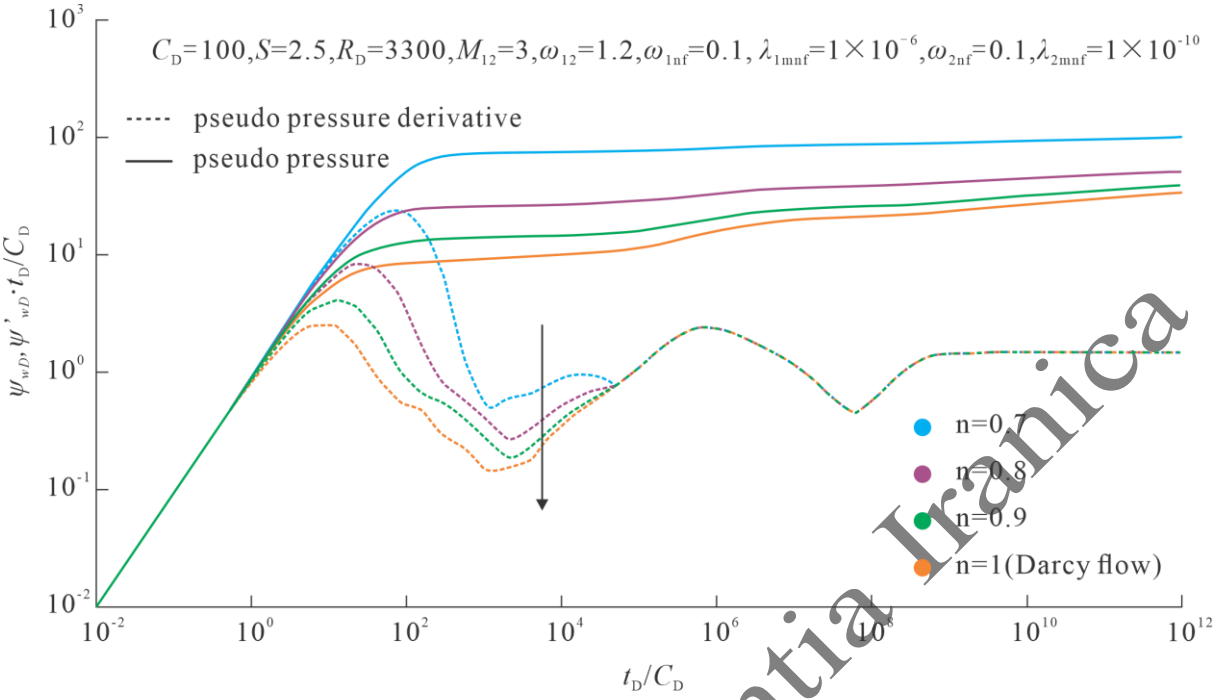

Figure 4 Influence of the radius of the high-speed non-Darcy region

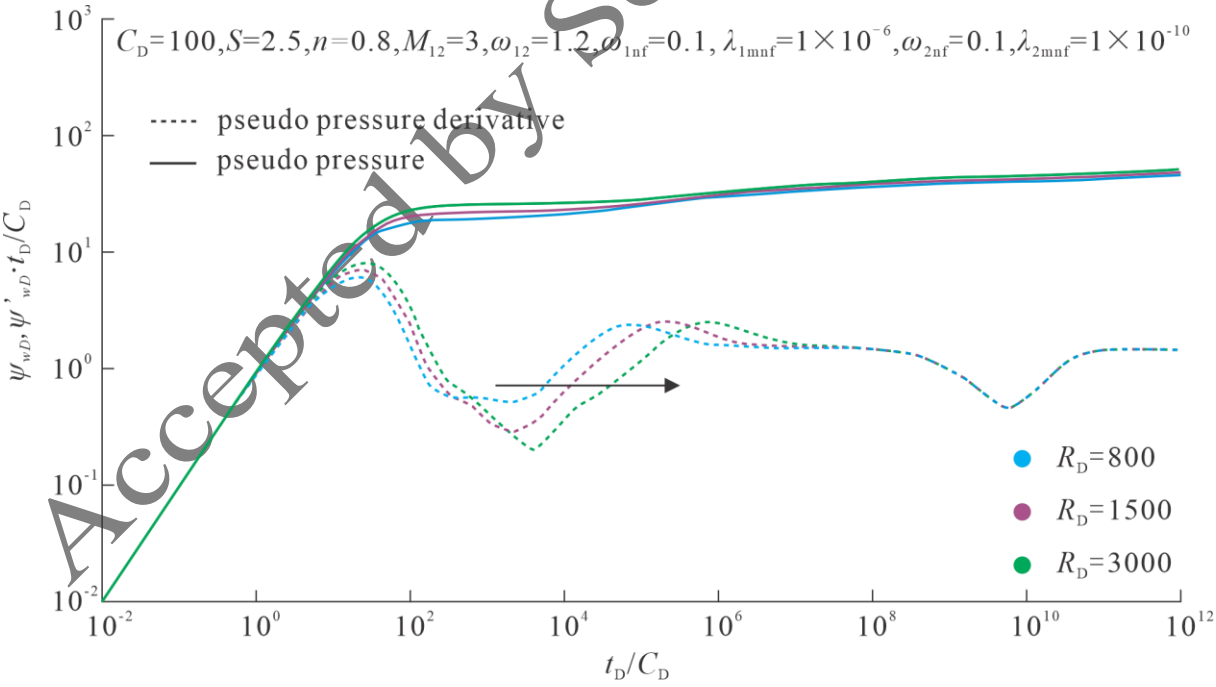

Figure 5 Influence of the fracture storage ratio

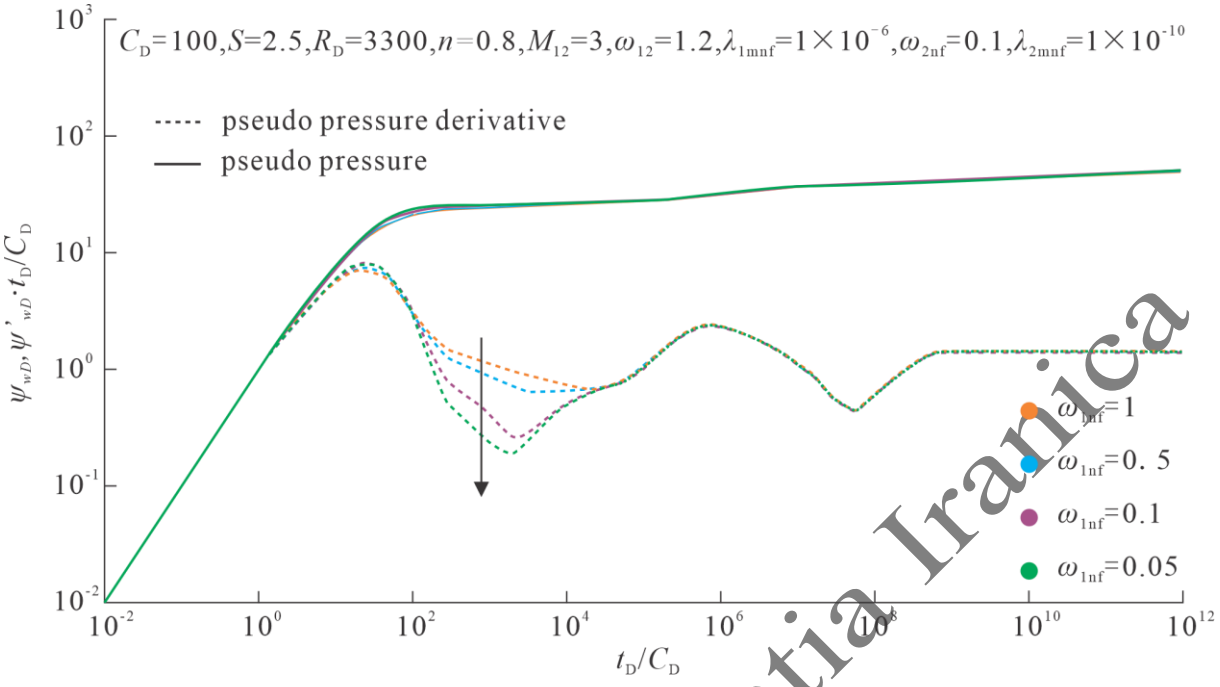

Figure 6 Influence of the crossflow coefficient in non-Darcy region

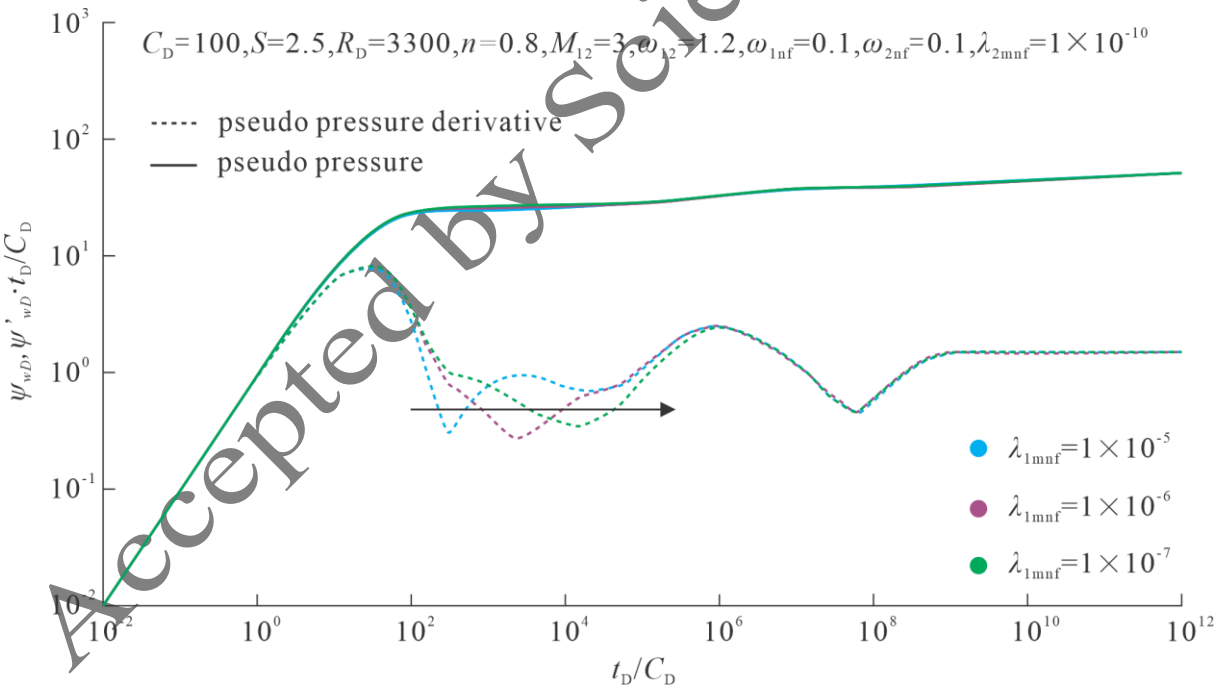

Figure 7 Influence of the mobility ratio

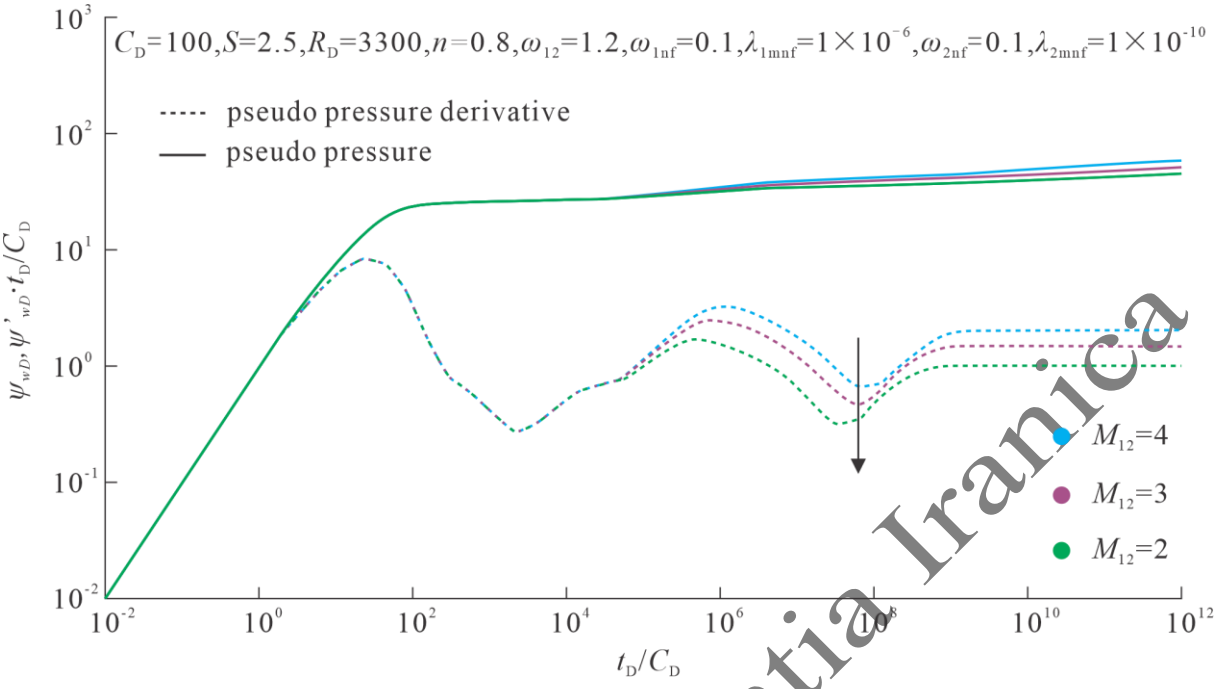

Figure 8 Influence of the storage coefficient

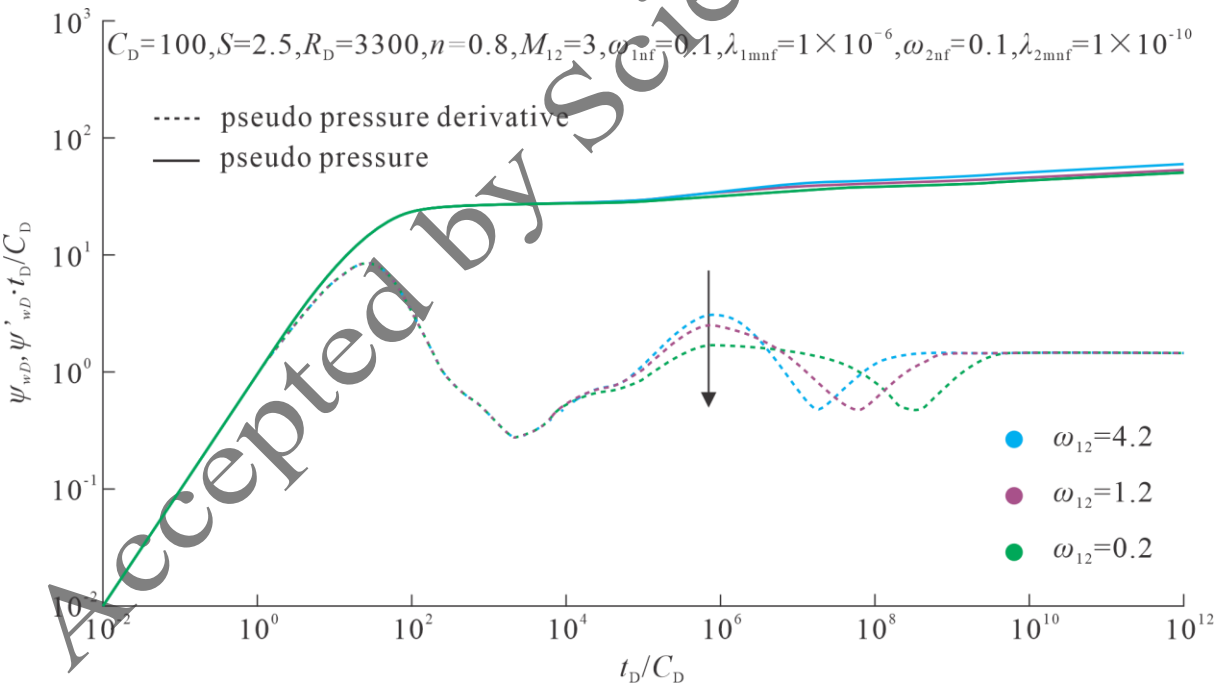

Figure 9 Influence of the fracture storage ratio in the Darcy region

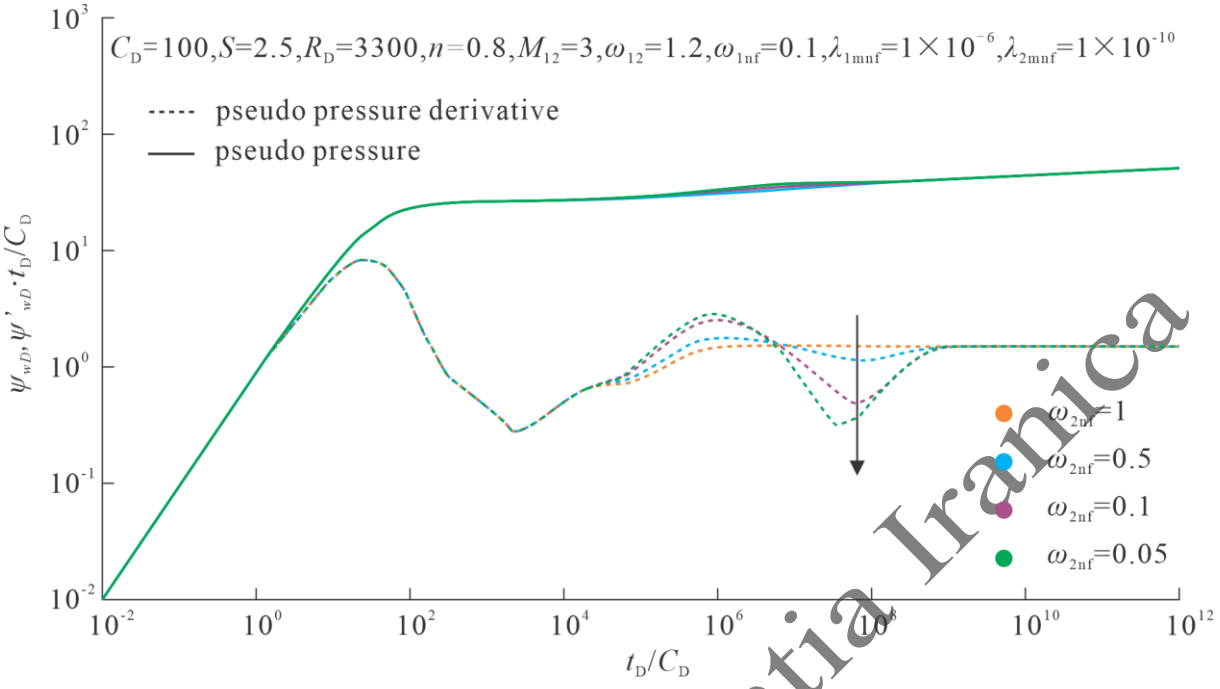

Figure 10 Influence of the crossflow coefficient in the Darcy region

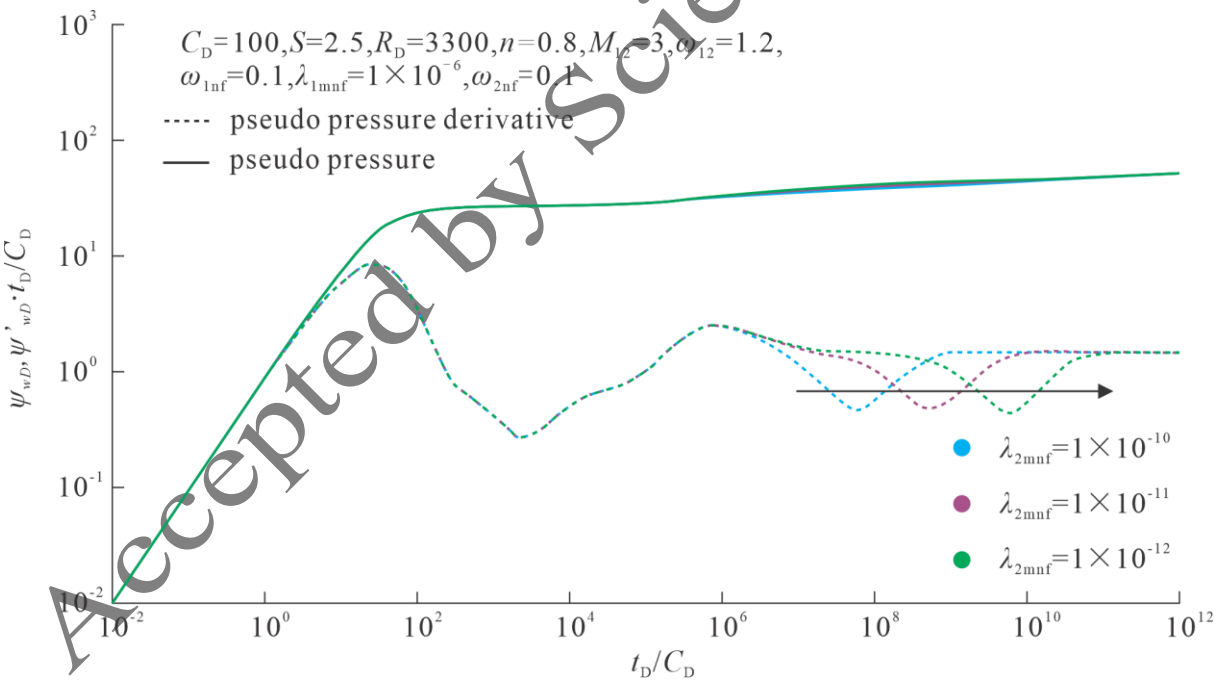

Figure 11 Well GS3 test fitting comparison

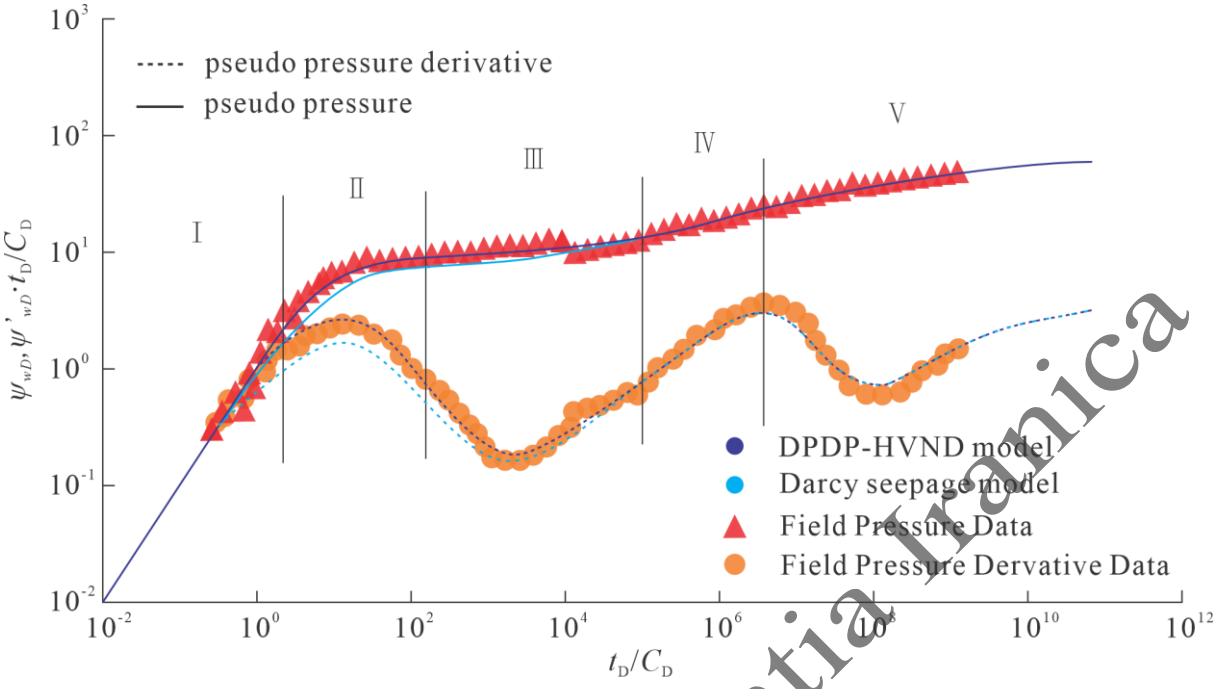

Table 1 The basic parameters of the example well.

wellbore radius (m)	Gas reservoir thickness (m)	Porosity (%)	Middle depth (m)	Relative density
0.062	28.5	0.0553	5037.6	0.61

Table 2 The fitting results of the example well.

Well bore storage constant, C (m^3/MPa)	Skin factor, S	Empirical constant, n	Crossflow coefficient, λ_{1mnf}	Crossflow coefficient, λ_{2mnf}	Storage ratio, ω_{1nf}	Storage ratio, ω_{2nf}
3.27	-1.38	0.91	6.35×10^{-5}	1.32×10^{-5}	0.082	0.16